Classification of synthetic platelets in digital holographic microscopy by neural network

K. F. TAMRIN*,[1], B. RAHMATULLAH[2]

[1]*Department of Mechanical and Manufacturing Engineering, Faculty of Engineering, Universiti Malaysia Sarawak (UNIMAS), 94300 Kota Samarahan, Sarawak, Malaysia.*

[2]*Computing Department, Faculty of Arts, Computing and Creative Industry, Sultan Idris Education University (UPSI), 35900 Tanjong Malim, Perak, Malaysia*

*Corresponding author: Email: tkfikri@unimas.my (K.F. Tamrin) | Tel: +601115653090 | Fax: +6082583410

Abstract

Automatic classification of cell types and biological products are considered crucial in the field of hematology especially for early detection of diseases when the quantity that needs to be examined is considerably large. In a previous study, a cylindrical micro-channel was employed to mimic actual blood flow in the arteriole but it was found to cause astigmatism in the reconstructed holographic particle images. Additionally, correction of the images is important to avoid false disease detection. In this paper, we describe a new application of feed-forward backpropagation neural network for classifying images of astigmatic and non-astigmatic synthetic platelets that were obtained by digital holographic microscopy. Image cropping was performed to suppress noise, followed by image normalization to reduce variation in contrast/brightness. Using MATLABTM, a two-layer neural network with two class classifier was trained with these images to compute the weights of each layer and the performance was benchmarked against three performance indices. The results show that the present method was able to classify 1050 platelet images with 100% recognition rate for Class 1 (non-astigmatic) and 71.4% recognition rate for Class 2 (astigmatic). The trained neural network was then applied to a set of 9000 images. Finally, digital aberration correction by complex-amplitude correlation was successfully applied to correct for the astigmatism.

1. Introduction

Digital holographic microscopy is one of the potential three-dimensional (3D) optical imaging techniques for real-time, non-invasive investigation of cells (Kemper & von Bally, 2008; Khmaladze et al., 2012; Pavillon et al., 2012) and microorganisms (Javidi, Moon, Yeom, & Carapezza, 2005; Lee, Seo, Choi, & Sohn, 2011; Shin, Daneshpanah, Anand, & Javidi, 2010). It is essentially an integration of digital holography and microscopy. The technique uses coherent light to illuminate a semi-transparent object in which the light (phase and amplitude) get modulated due to light-matter interaction. This interaction is recorded using imaging sensors in the form of complex interference fringes or simply known as digital hologram, which can be digitally processed to reconstruct the entire three-dimensional volumetric field from a single hologram capture (Tamrin & Rahmatullah, 2016). However, the amount of data available is considerably enormous and laboriously challenging to deal with manually. Alternatively, a number of studies have shown the use of statistical pattern recognition techniques for automatic recognition, classification and tracking of images acquired using digital holographic microscopy with remarkable results.

Frauel and Javidi (2001) demonstrated for the first time the application of neural network for 3D pattern recognition from digital holograms. Through supervised neural network using 36 composite filters (each filter corresponds to a predefined rotation), they showed how digital holograms of the same object with 36 different rotations can be correctly classified with good accuracy (minimum error < 1%) despite strong correlation peaks between them. The strong correlation peaks (indication of similarities) at different rotations were attributed to the use of one single object.

Studies have shown that the risk after blood transfusion increases with the increase of storage duration where the preserved blood cells may suffer structural and functional degradations (Koch et al., 2008; Tinmouth, Fergusson, Yee, & Hébert, 2006). Following this, Liu, Dey, Boss, Marquet, and Javidi (2011) compared two statistical clustering algorithms to recognize and classify 3D profile of red blood cells based on their duration of storage, acquired using digital

holographic microscopy. In a supervised model-based clustering algorithm (Fraley & Raftery, 2002), three old RBCs and three new RBCs were chosen for training samples, and 17 old RBCs and 17 new RBCs were chosen for testing samples. The corresponding rates of success for old and new RBCs were 76.5% and 100%, respectively. Liu et al. (2011) attributed shrinkage with the increase of age in the old RBCs as the main reason for low success rate. On the other hand, the rates of success using unsupervised K-means clustering algorithm (Hartigan & Wong, 1979) were 80% and 95% for old and new RBCs, respectively.

In some instances, white blood cell count and its morphology were discovered to have profound effects on certain diseases (Ladhani, Lowe, Cole, Kowuondo, & Newton, 2002; Yarnell et al., 1991). Schneider, Vanmeerbeeck, Stahl, Lagae, and Bienstman (2015) employed an optical neural network in digital in-line holographic microscopy for classification of three types of white blood cells namely, granulocytes, lymphocytes and monocytes. By incorporating a flow cytometer in the holographic microscope, blood cells can be precisely aligned so that only one single cell is permitted to pass through the imaging system at a time for cell characterization and counting purposes. In that instant, the holographic microscope recorded interference fringes corresponding to one particular type of cell and the input data was fed in the forward direction and subsequently weighed through the optical neural network. Thereafter, a decision signal was sent to the cytometer to selectively channel the cell to its collection outlet. The same step was repeated for the next cell in line which flowed at speed of more than 100 cm/sec. The study interestingly demonstrates label-free and high speed classification of cells in real-time using digital holographic microscopy with 90% accuracy.

Moon, Javidi, Yi, Boss, and Marquet (2012) presented an automated approach to quantify information about 3D patterns of mature red blood cells (RBCs) using quantitative phase images obtained by off-axis digital holographic microscopy. The study was limited to two types of RBCs namely, stomatocyte and discocyte, which were stored for 14 and 38 days, respectively. Of many attributes available from the phase images, only five were measured: projected cell surface, average phase, mean corpuscular haemoglobin (MCH) and mean corpuscular haemoglobin surface density (MCHSD). Based on nearest neighbour classification technique, each cell can be classified to its group by comparing the average value of all attributes with the total mean value from each class. The cell was then assigned to the respective class accordingly.

Recently, Tamrin, Rahmatullah, and Samuri (2015b) studied three-dimensional aggregation of therapeutic platelet substitutes which was clinically developed for leukaemic patients who generally suffers platelet deficiency as a consequence of chemotherapy treatment. Since platelets aggregation is heavily influenced by the surrounding hemodynamic environments (Ha & Lee, 2013), the experiment utilised a transparent PVC-based circular micro-channel to simulate arteriole blood flow as closely as possible. This unfortunately introduced astigmatism in some of the reconstructed particle images out of 9000 images. In the present study, a feed-forward backpropagation neural network (Beale, Hagan, & Demuth, 1992) is applied to automatically classify these images prior to digital aberration correction . This study is deemed crucial in the field of hematology especially in the early detection of blood disorders (e.g., anemia) and blood cancers (e.g., leukemia). The experimental setup is discussed in the following section.

2. Methodology

2.1. Experimental setup

Figure 1 illustrates the optical diagram of an off-axis digital holographic microscope developed previously by Wormald and Coupland (Wormald & Coupland, 2009). The working principle of the holographic microscope has been described in (Tamrin et al., 2015b; Wormald & Coupland, 2009). It consists of a diode pumped solid state Nd:YLF laser (wavelength, $\lambda = 523$ nm, manufactured by Elforlight Ltd., UK). The laser beam is split into a reference wave and an object wave. On the beam path, the light scattered by the particles was collected using a Mitutoyo M Plan 50x long working distance with numerical aperture, NA = 0.55. The object beam later interferes with the reference wave in the off-axis geometry (intersecting angle = θ_{ccd}) to produce the hologram recorded on a 10 Megapixel Lumenera CCD camera with resolution of 4008 x 2672 pixels. After demodulation, the hologram was reduced to 1200 x 800 pixels with 0.37 µm spacing.

(a)
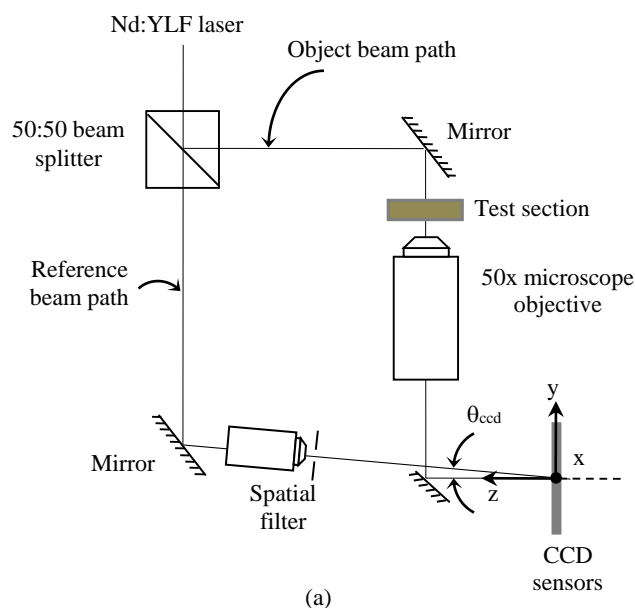
Figure 1: Optical diagram of a digital off-axis forward-scatter holographic microscope used for the experiment.

Figure 2 shows the cross-sectional view of the test section. To mimic arteriole blood flow as closely as possible, a transparent micro-channel (TygonLab R-3603) was used, embedded with an index matching fluid to minimize aberration. The experimental configuration was used to make holographic recordings of the particles in the micro-channel at time t = 4, 8, 16, 32, 64 minutes, and t = 1 day. A detailed experimental procedure has been described in (Tamrin et al., 2015b). The 3D centroid positions of the particles and their images at the plane of focus were acquired using a novel particle image identification technique within a predefined interrogation volume size of 234 μm (width) x 367 μm (length) and 400 μm (height). The number of identified particle image was limited to 1500 particles for each recording exposure to avoid detecting noise (Tamrin et al., 2015b). In total, 9000 reconstructed particle images were extracted from six different recording intervals. It was found that some of the identified particles were influenced by astigmatism but the actual number was not quantified particularly due to massive amount of images that need to be examined. Here, we resort to pattern recognition using neural network to facilitate particle image classification.
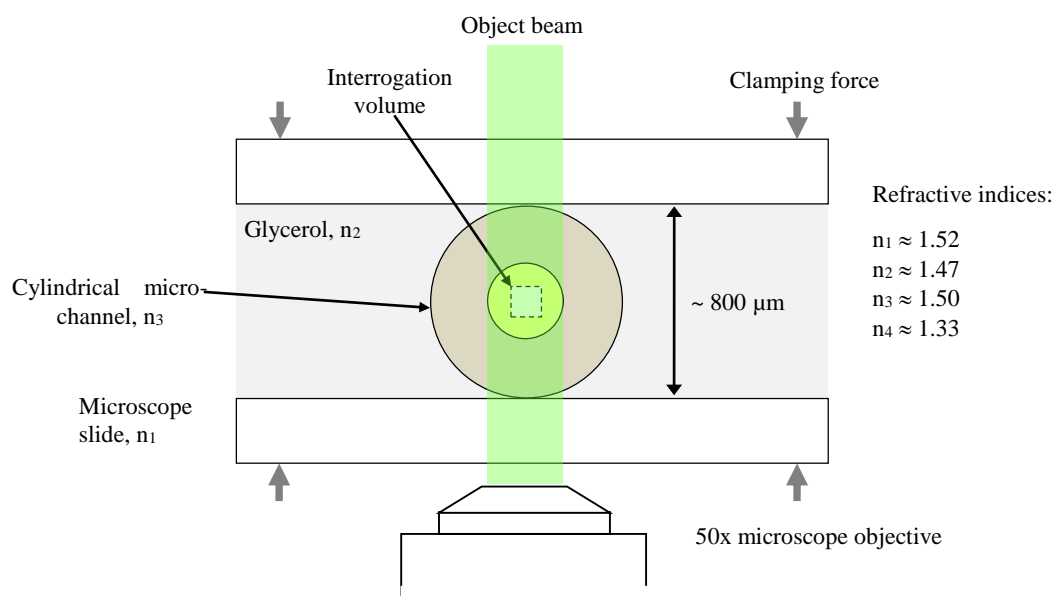

Figure 2: Cross-sectional view of the test section and refractive indices of the media.

2.2. Classification of synthetic platelets images by feed-forward backpropagation neural network

The feed-forward backpropagation neural network is one of the most typical neural network architectures. It has received wide acceptance in various applications because of its strength to cope with non-linear solutions in complex multi-layer networks (Basheer & Hajmeer, 2000; Hagan & Menhaj, 1994; Zhang, Zhang, Lok, & Lyu, 2007).

2.2.1. Feed-forward backpropagation network

In a feed-forward neural network, neurons are only connected in the forward direction with no feedback between layers. A network that is trained using backpropagation training algorithm overcomes the former main limitation. Backpropagation is a type of supervised training. Initially, the network must be supplied with some sample inputs and their anticipated outputs (targets). Later, for a given input, the predefined target is compared against the output generated by the neural network. The difference between target and output is calculated as "error". By considering the error generated, the backpropagation training algorithm then modifies the weights of the various layers backwards from the output layer to the input layer, as illustrated in **Figure 3a**. In this study, the back propagation algorithm was based on Levenberg-Marquardt in which, the weight adjustment is measured based on mean squared error (MSE) (Beale et al., 1992). In the initialization step, a random weight was imposed on the network and the corresponding error was computed. This gives an indication how the initial weight should be corrected. The same process was repeated in the neural network until the minimum value of error was obtained.

As shown in **Figure 3b**, the neural network used in this study comprises of two layers. The first layer, or hidden layer, has a linear activation function, and the second layer, or output layer, has a tan sigmoid (tan-sig) activation function. In this way, the first linear layer of the network outputs can take on any value while the outputs of the second layer are limited to a small range due to sigmoid neurons.
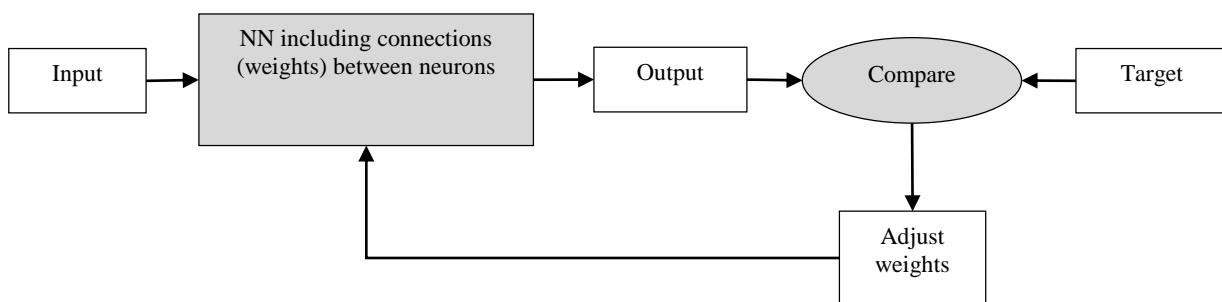

(a)
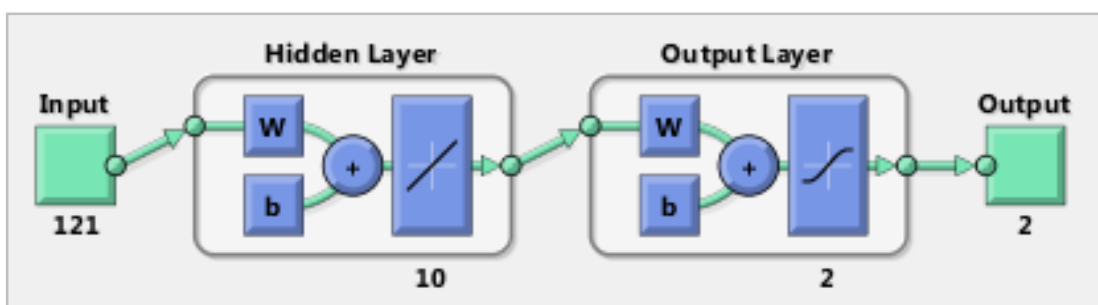
(b)

Figure 3: (a) Block diagram for training of neural network. (b) Diagram of the neural network consisting of 121 inputs (cropped image of 11 by 11 pixels) and two outputs (Class 1, Class 2).

2.2.2. Data pre-processing

In the previous work (Tamrin et al., 2015b), there were 1500 particles identified using the novel particle image identification algorithm and their images were stored in a database. The size of each image is 41x41 pixels and was cropped to a smaller image size of 11x11 pixels, as shown in **Figure 4**. This step effectively reduces computational load. It also removes neighbouring noise and neighbouring particle images which could affect the accuracy of the neural network.

In addition, each pixel in the image was normalized to grayscale of 0 to 225, eliminating variation in contrast and brightness between various particle images, using the following equation:

$$I_{p,n} = \frac{\left(I_p - I_{min,image}\right)}{\left(I_{max,image} - I_{min,image}\right)} \times 255 \tag{1}$$

where $I_{p,n}$ is the normalized local intensity, I_p is the local intensity, $I_{max,image}$ and $I_{min,image}$ are the respective highest and lowest intensity in the image, and $p = [1, 2, 3, …., 121]$. This helps neural network to recognise the pattern corresponding to good and astigmatic particle image.

Original image size 41x41 pixels

Cropped image size 11x11 pixels

Example:
$I_{p=61}$ = abs(212.35 + 794.25i) = 822.15
$I_{61,n}$ = (822.15 − 11.66) x 255 ÷ (822.15 − 11.66) = 255

Figure 4: One of the original images (41x41 pixels) obtained using digital holographic microscopy was cropped to smaller image size of 11x11 pixels. Each pixel carries amplitude and phase information, and the absolute intensity is then normalized from 0 to 255. The pixel is then arranged accordingly, forming the input layer of the neural network with 121 neurons.

Table 1: Specifications of neural network

	Parameter	Value
1	Type of network	Feed-forward back propagation
2	No. of neurons in the input layer	121
3	No. of neurons in the hidden layer	10

4	No. of neurons in the output layer	2
5	Performance function	MSE
6	Activation function in the hidden layer	tan-sigmoid
7	Activation function in the output layer	purelin
8	Learning rate	0.001
9	Maximum no. of epochs	9
10	Minimum MSE value	
11	Training parameters ratio	69.90%

Initially, 1050 dataset of random particle images were manually scrutinized and classified into two different classes: (a) Class 1 (good), and (b) Class 2 (astigmatic). The dataset was randomly distributed as follows:

i.   734 images for training (69.9%)

ii.   158 images for validation (15.05%), and

iii.   158 images for testing (15.05%)

2.2.3. Performance analysis

The neural network performance used for the classification process was evaluated using the following three performance indices:

2.2.3.1. Mean squared error

Mean squared error (MSE) was computed by averaging the squares of the errors i.e., the differences between the targets, T_i and the actual neural network outputs, O_i (Beale et al., 1992) as written in Equation (2).

$$\text{MSE} = \frac{1}{p}\sum_{i=1}^{p}(T_i - O_i)^2$$

(2)

The performance plot of the mean squared error (MSE) is shown in **Figure 5** and it is usually used to indicate the iteration at which the validation performance reached a minimum. The curves representing the training, validation and testing appear normal with no reported spike as the iteration increases. In other words, there is no overfitting in the trained algorithm for 1089 (121 inputs x 9 epochs) individual training trials.
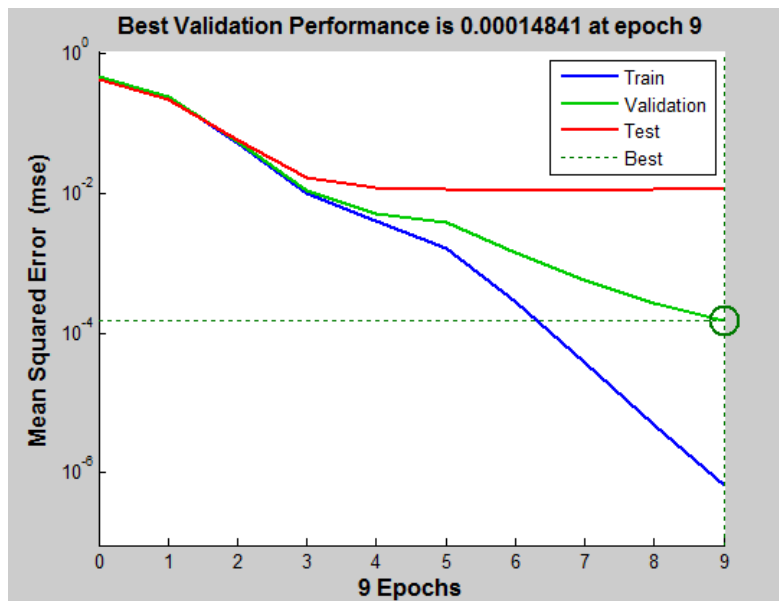
Figure 5: The performance plot of the mean squared error (MSE) is usually used to indicate the iteration at which the validation performance reached a minimum.

2.2.3.2. Confusion matrix

A two-by-two (two class classifier) confusion matrix was constructed to assess the performance of the trained NN at distinguishing good and astigmatic images, as shown in **Figure 6**.

Figure 6: Confusion matrix: green and red shaded cells represent correct and incorrect classifications, respectively. All 1043 good samples were correctly classified as Class 1. On the other hand, five astigmatic samples were correctly classified as Class 2 while the remaining two samples were mistakenly identified as Class 1.

The confusion matrix indicates:

a)   1043 true positives (actual good images that were correctly classified as good)

b)   No false negative (actual good images that were incorrectly classified as astigmatic)

c)   2 false positives (actual astigmatic images that were incorrectly classified as good)

d)   5 true negatives (actual astigmatic images that were correctly classified as astigmatic)

It is noted that the overall accuracy of the trained NN is 99.8% whereby it has 100% recognition rate for Class 1 but 71.4% recognition rate for Class 2. The apparently high overall accuracy could be the result of data set imbalance where there were 1043 good samples available as compared to 7 astigmatic samples.

2.2.3.3. Regression plot

Regression plots showing the relationship between the output of the neural network and the targets for training, validation and testing data are given in **Figure 7**. The dashed line in each plot represents the perfect result, where the outputs exactly match the targets. The solid line represents the best fit linear regression line between outputs and targets. The R value is an indication of the relationship between the outputs and targets. An exact linear relationship between outputs and targets is acquired when R = 1. If R is close to zero, then there is no linear relationship between outputs and targets. In this analysis, the training data indicates a perfect fit (R=1), indicating an exact relationship between outputs and targets. The validation and test results also show R values that are greater than 0.95. Additionally, there are two data points in the scatter plot showing incorrect classification, as indicated by dotted circles. This result is consistent with the finding shown in the confusion matrix.
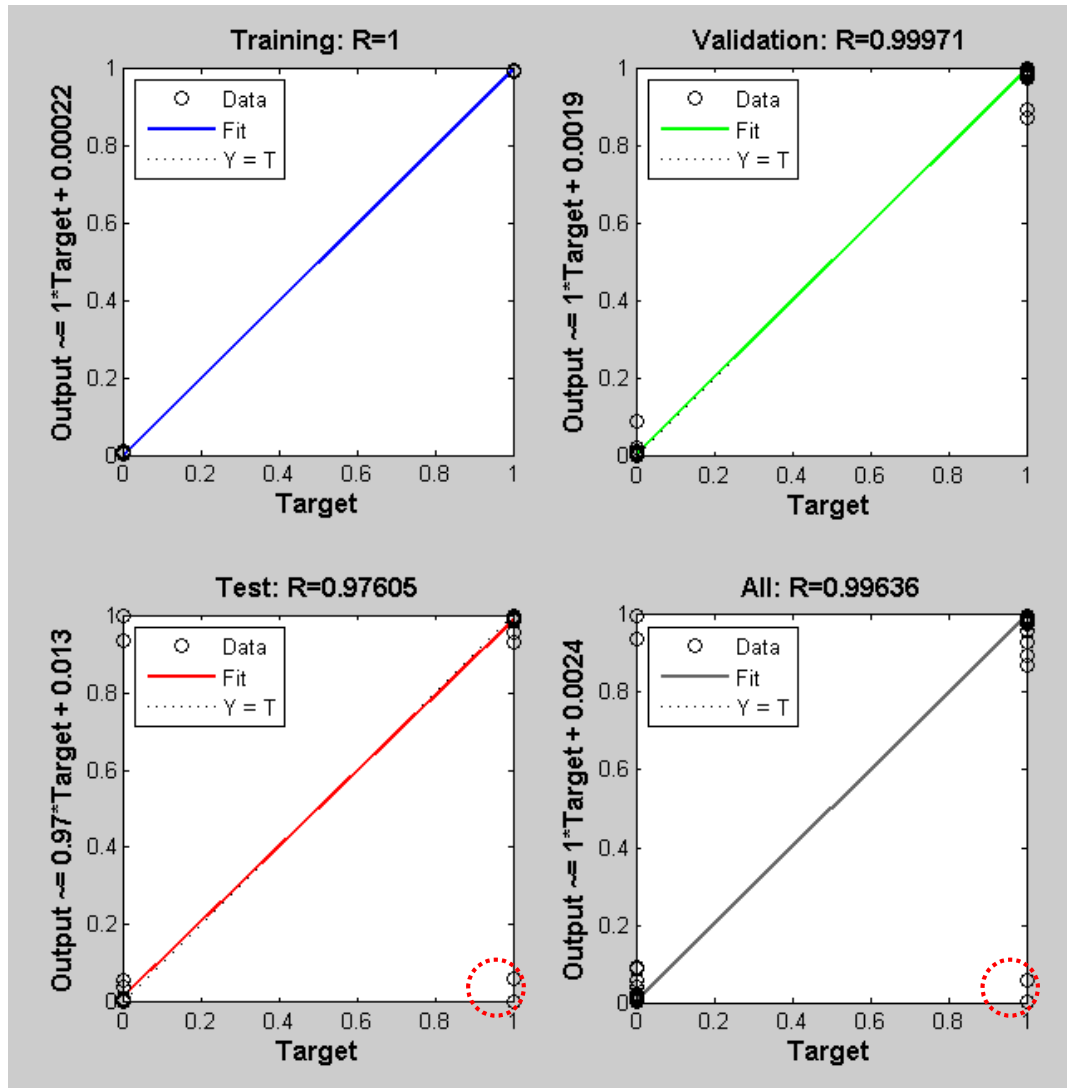
Figure 7: Regression plots showing the relationship between outputs and targets for training, validation and testing data.

3. Results and discussion

3.1. Results

Thereafter, the trained neural network was used to simulate classification of 9000 images. Astigmatic images with classification accuracy greater than 50% were manually examined to re-confirm the present of astigmatism. Some of the correctly classified astigmatic images are shown in **Figure 8**. Additionally, this step is deemed important to compensate for any error inherent in the trained NN that could be the consequence of limited astigmatic images available for the training as discussed in Section 3.0. In general, the trained NN:

a) correctly identified 21 astigmatic particle images. These were images with classification accuracies greater than 50% and they also passed the subsequent manual inspection.
b) falsely identified an image as astigmatic with a reported classification accuracy of 86.4%. As shown in **Figure 9**, there were two particles located in close proximity in which one of the particles has a black circular mask (Tamrin et al., 2015b). The mask applied to the neighbouring particle image leaves a footprint that causes the particle image in the centre to appear in the shape of astigmatic.
c) failed to identify the same two astigmatic images used previously in the training set (see **Figure 10**). This is consistent with the findings shown in the confusion matrix and regression plots.
d) In total, there were 23 astigmatic particles images out of a collection of 9000 images, as listed in **Table 2**.
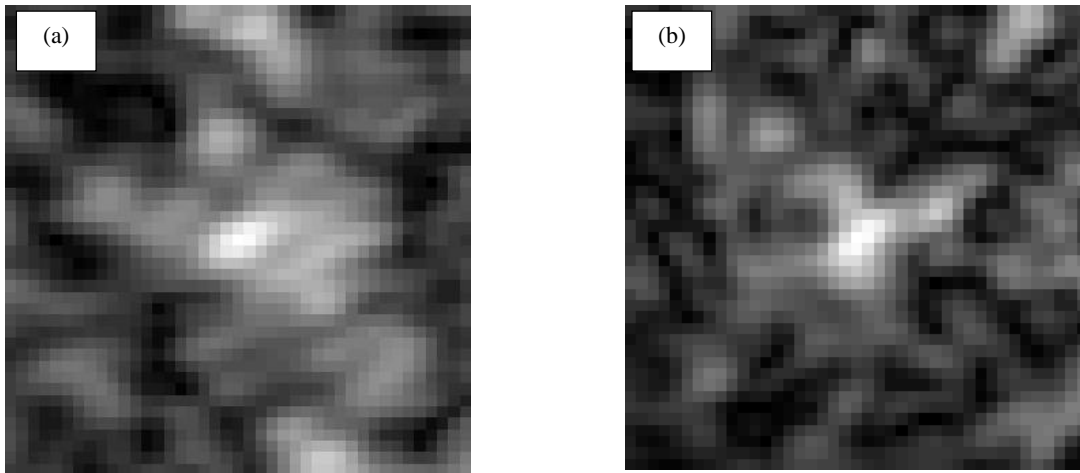
Figure 8: Astigmatic particle images with classification accuracies greater than 50% were subjected to manual inspection: (a) 55.7% (Exp4_4min no. 561) and (b) 65.3% (Exp4_32min no. 775).

Footprint of the mask applied to the nearby image
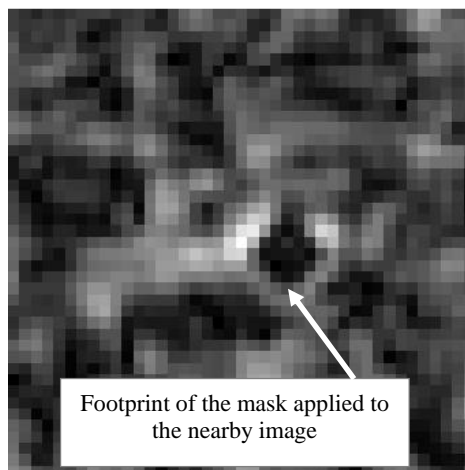
Figure 9: The trained NN falsely identified the above image as astigmatic with a reported classification accuracy of 86.4% (Exp4_16min no. 106). A footprint of the mask applied to a neighbouring particle image causes it to appear astigmatic.
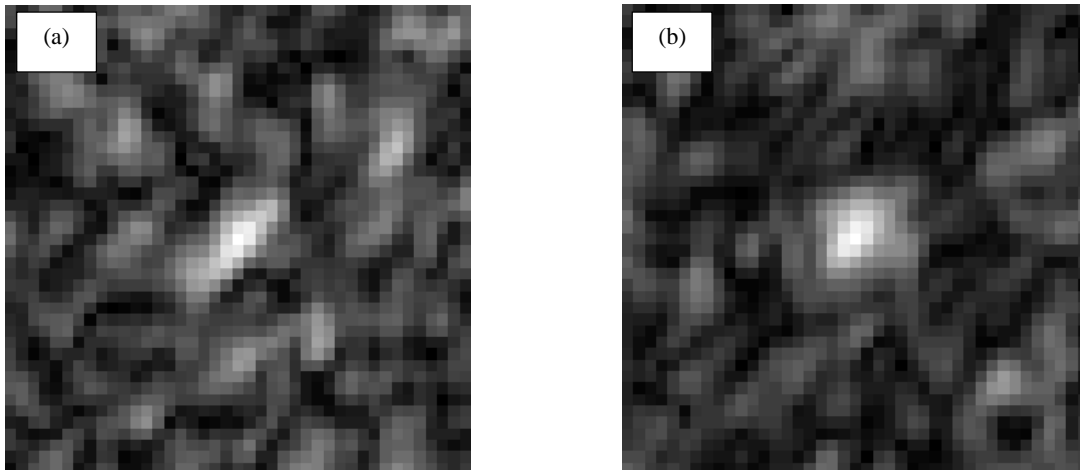
Figure 10: The trained NN failed to identify the astigmatic particle images: (a) (Exp4_32min no. 293), and (b) (Exp4_8min no. 206).

Table 2 lists the 3D positions of the astigmatic particle images classified using the trained NN while their 3D positions within the interrogation volume are plotted in **Figure 11**. Any image with classification accuracy greater than 90% can be considered as severely astigmatic. On the other hand, the influence of astigmatism is less severe for images with classification accuracy in the interval of 50% to 90%. It can be seen that majority of the astigmatic particle images appear closer to the bottom and nearer to the wall boundary. These locations are expected to be highly influenced by astigmatism and becoming more severe further away from the central axis of the micro-channel. Based on 3D particle distribution of the images, both severe and less severe images accommodate many common section of the interrogation volume. Therefore, it cannot be established that the severity of astigmatism is location-dependent.

Table 2: The 3D positions of the astigmatic particle images identified using the trained NN

|	Experiment (Particle no.)	Actual coordinate measured from origin (0,0,0)	Classification accuracy, c (%)
1	Exp4_4min (561)	(167.6, 71.0, 146)	55.7
2	Exp4_4min (1468)	(152.1, 263.8, 300)	53.9
3	Exp4_8min (5)	(207.6, 314.1, 278)	99.6
4	Exp4_8min (206)	(67.3, 280.1, 28)	0.1
5	Exp4_8min (423)	(187.6, 225.3, 164)	70.5
6	Exp4_8min (481)	(199.8, 270.1, 332)	54.1
7	Exp4_8min (801)	(170.9, 125.8, 366)	59.2
8	Exp4_8min (1431)	(170.2, 316.7, 318)	80.7
9	Exp4_8min (1449)	(188.7, 222.0, 222)	58.9
10	Exp4_32min (237)	(99.2, 378.5, 42)	99.4
11	Exp4_32min (293)	(96.9, 290.1, 108)	5.8
12	Exp4_32min (336)	(198.3, 87.3, 126)	99.9
13	Exp4_32min (775)	(198.3, 84.0, 152)	65.3
14	Exp4_32min (855)	(141.3, 108.4, 308)	62.5
15	Exp4_32min (1339)	(207.6, 314.1, 278)	91.8
16	Exp4_64min (266)	(197.2, 117.7, 120)	79.0
17	Exp4_64min (907)	(115.8, 367.8, 134)	57.8
18	Exp4_1day (1)	(113.2, 327.1, 124)	98.6
19	Exp4_1day (49)	(116.2, 327.1, 124)	99.7
20	Exp4_1day (1097)	(88.4, 107.7, 24)	50.3
21	Exp4_1day (1115)	(89.5, 354.8, 46)	64.0
22	Exp4_1day (1431)	(161.7, 100.6, 292)	67.6
23	Exp4_1day (1461)	(141.7, 308.6, 258)	63.5
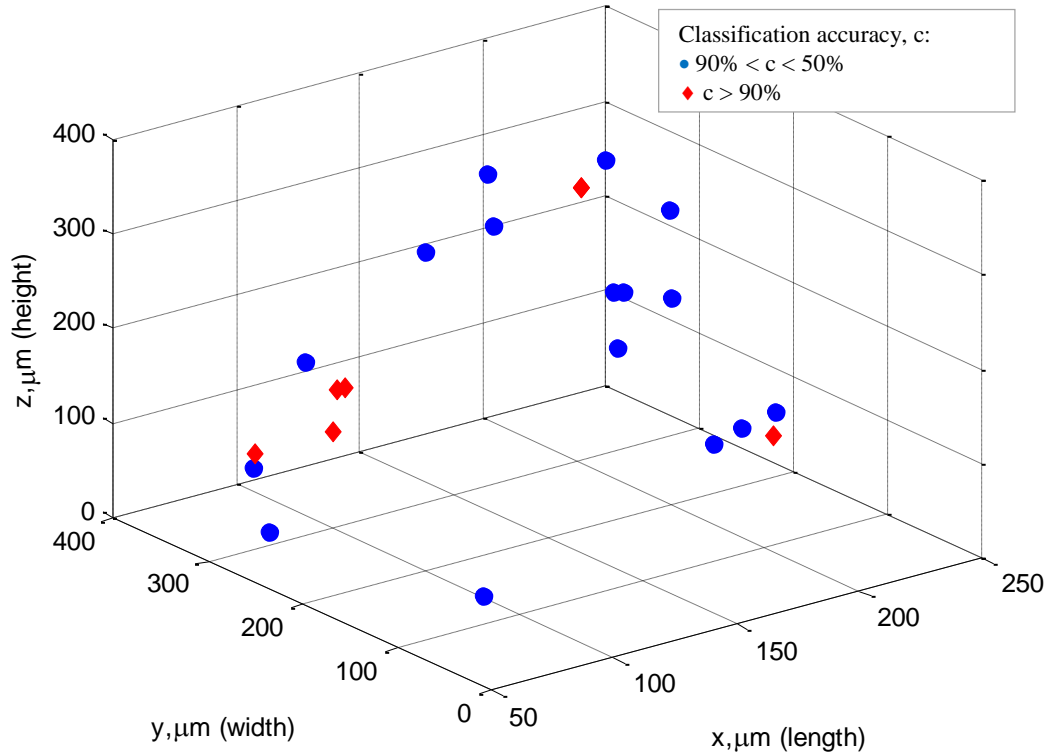
Figure 11: 3D distribution of astigmatic particle images within the interrogation volume. Majority of the particles are located closer to the bottom and nearer to the wall boundary i.e., further away from the central axis of the micro-channel.

3.1.1. Digital aberration correction

To correct for the astigmatism in the particle images, a digital aberration correction technique as described in (Tamrin, Rahmatullah, & Samuri, 2014, 2015a) was employed. The technique makes use of *a priori* information of the geometry and orientation of the cylindrical micro-channel to estimate the wavefront aberration in the form of quadratic phase function. An original wavefront aberration introduced by the micro-channel in the plane of the hologram (x,y) can be modelled as a quadratic phase function, θ, such that

$$\theta = a_0 \left(a_1 x + a_2 y + a_3 \right)^2 \tag{3}$$

where a_0, a_1, a_2 and a_3 are constants. These constants depend on *a priori* information particularly the orientation of the micro-channel in the x-y plane (a_1 and a_2), its diameter (a_0), and shift of the centre of the micro-channel from the origin (a_3). Following this, the corresponding complex amplitude of the quadratic phase function can be defined as:

$$U_\theta(x, y) = e^{-j\theta(x,y)} = e^{-j a_0 \left(a_1 x + a_2 y + a_3 \right)^2} \tag{4}$$

To correct for the astigmatism, the complex amplitude of the particle image, $U_{obj}(x,y)$ is convolved with the conjugate of the estimated phase function in Equation (4) such that

$$U_{comp}(x, y) = U_{obj}(x, y) \otimes e^{j a_0 \left(a_1 x + a_2 y + a_3 \right)^2} \tag{5}$$

Then, a reconstruction of the entire 3D image (Tamrin et al., 2015b) with peak detection algorithm is performed through convolution operation between the spectrum (Equation (5)) with a spherical phase function in *k*-space . The correction results concerning astigmatic particle images having classification accuracies greater than 90% are demonstrated in **Figure 12**.

Original image (41x41 pixels)	High-contrast image (41x41 pixels)	High-contrast image after astigmatism correction (41x41 pixels)
	(a) (Exp4, t = 8 min, *i* = 5)	
	(b) (Exp4, t = 32 min, *i* = 237)	
	(c) (Exp4, t = 32 min, *i* = 293)	
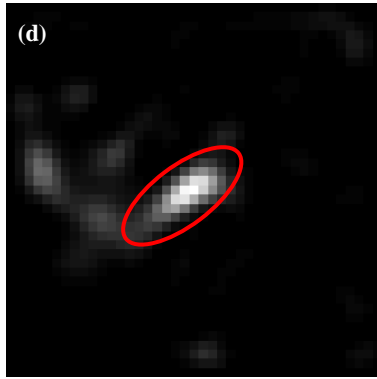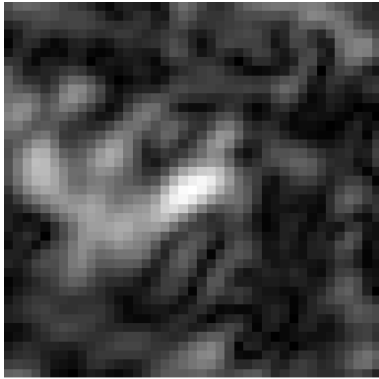
(d) (Exp4, t = 32 min, *i* = 336)
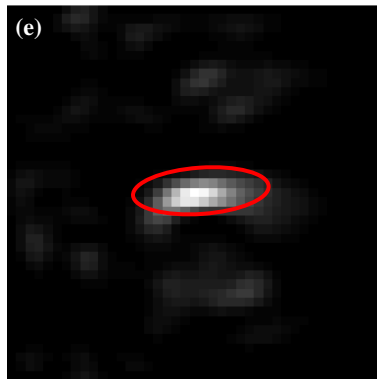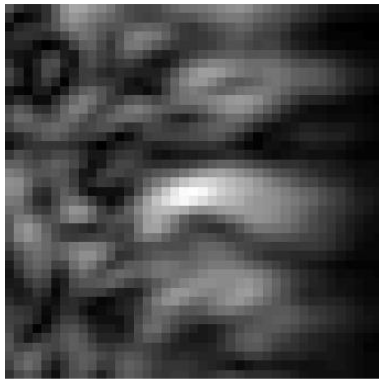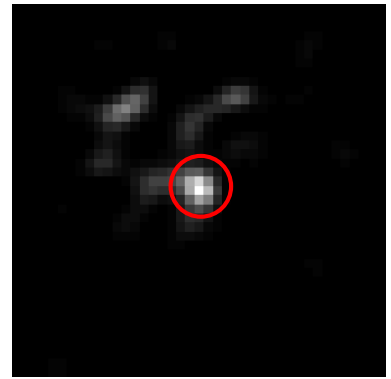
(e) (Exp4, t = 32 min, *i* = 1339)
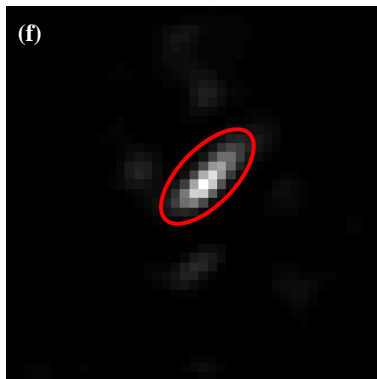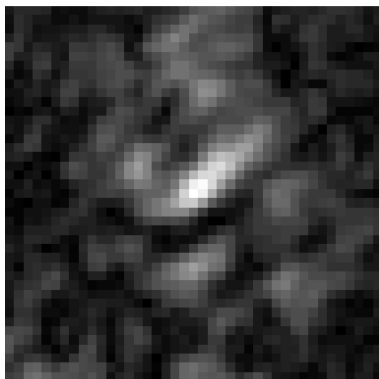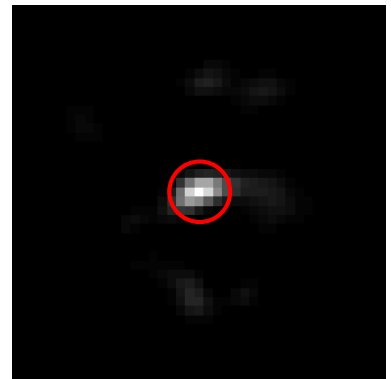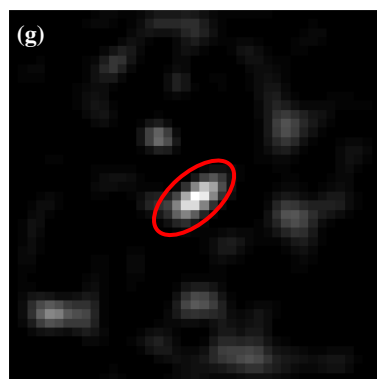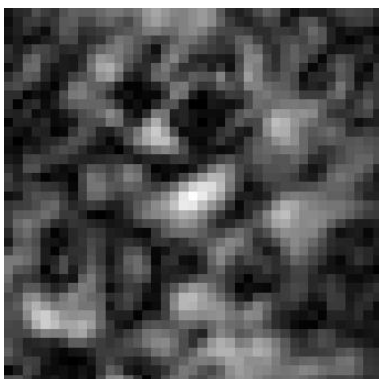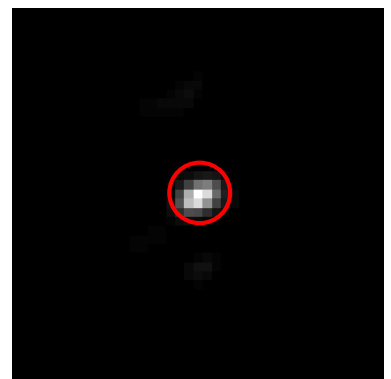
(f) (Exp4, t = 1 day, *i* = 1)

(g) (Exp4, t = 1 day, *i* = 49)
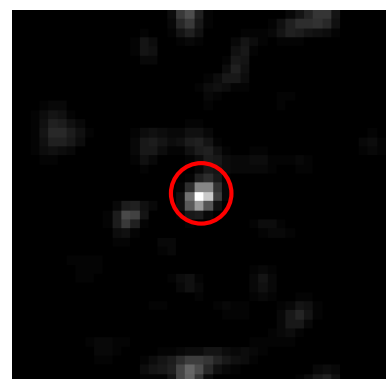
Figure 12: Left column shows astigmatic particle images with classification accuracy greater than 90%. Middle column shows the high-contrast of the same images. Right column shows the high-contrast of the same images after astigmatism correction. Note: Peak centroid is located at the centre of the image.

3.2. Discussion

It is imperative to note that any supervised image classification of a considerably large amount of images is inherently complex where its performance and accuracy rely upon the training data supplied (Kavzoglu, 2009). To ensure that the input layer has been optimized, we further tested the procedures discussed in Section 3.2 for binary image using the same configuration of neural network as listed in **Table 1**. Each image was normalized from 0 to 255 with a threshold value of 200. The result indicates that the trained NN failed to identify any astigmatic particle image. In a separate analysis, the binary image was substituted with high-image contrast (normalized with contrast and brightness adjustment). Similarly, in this case, not even a single astigmatic image managed to be detected.

An ideally corrected particle image should appear in the form of a single point at its peak intensity but this kind of pattern was not found visible in **Figure 12**. By referring to **Figure 2**, some of the reasons for this anomaly could be (a) shape deformation in the micro-channel due to uneven compression between two microscope slides, and (b) differences in refractive indices along the optical path. These elements are not straightforward to be accounted for in the mathematical model to form parts of the wavefront aberration.

4. Conclusions

Automatic and accurate image classification is deemed crucial in the field of hematology especially, in the early detection of blood disorders and blood cancers. In conclusion, this study has concerned the application of feed-forward backpropagation neural network for automatic image classification of synthetic platelets flowing inside a cylindrical micro-channel. From the total of 1050 training samples images obtained using digital holographic microscopy, only 7 astigmatic samples were available. Nevertheless, the overall accuracy of the trained neural network achieved was 99.8%, whereby the recognition rates for Class 1 (good) and Class 2 (astigmatic) were 100% and 71.4%, respectively. The trained neural network was further used to simulate classification of 9000 images. To minimise error due to data set imbalance and to re-confirm the present of astigmatism, manual inspection was performed on astigmatic images having classification accuracies greater than 50%, and 23 images were discovered to be in the particular class. We also successfully demonstrated the application of a digital holographic technique for correcting astigmatism in the severely affected particle images i.e., those original images (amplitude and phase) having classification accuracies greater than 90%.

References

Beale, M., Hagan, M. T., & Demuth, H. B. (1992). Neural network toolbox. *Neural Network Toolbox, The Math Works, 5*, 25.

Fraley, C., & Raftery, A. E. (2002). Model-based clustering, discriminant analysis, and density estimation. *Journal of the American statistical Association, 97*(458), 611-631.

Frauel, Y., & Javidi, B. (2001). Neural network for three-dimensional object recognition based on digital holography. *Optics letters, 26*(19), 1478-1480.

Ha, H., & Lee, S.-J. (2013). Hemodynamic features and platelet aggregation in a stenosed microchannel. *Microvascular research, 90*, 96-105.

Hartigan, J. A., & Wong, M. A. (1979). Algorithm AS 136: A k-means clustering algorithm. *Applied statistics*, 100-108.

Javidi, B., Moon, I., Yeom, S., & Carapezza, E. (2005). Three-dimensional imaging and recognition of microorganism using single-exposure on-line (SEOL) digital holography. *Optics Express, 13*(12), 4492-4506.

Kemper, B., & von Bally, G. (2008). Digital holographic microscopy for live cell applications and technical inspection. *Applied optics, 47*(4), A52-A61.

Khmaladze, A., Matz, R. L., Epstein, T., Jasensky, J., Holl, M. M. B., & Chen, Z. (2012). Cell volume changes during apoptosis monitored in real time using digital holographic microscopy. *Journal of structural biology, 178*(3), 270-278.

Koch, C. G., Li, L., Sessler, D. I., Figueroa, P., Hoeltge, G. A., Mihaljevic, T., & Blackstone, E. H. (2008). Duration of red-cell storage and complications after cardiac surgery. *New England Journal of Medicine, 358*(12), 1229-1239.

Ladhani, S., Lowe, B., Cole, A. O., Kowuondo, K., & Newton, C. R. (2002). Changes in white blood cells and platelets in children with falciparum malaria: relationship to disease outcome. *British journal of haematology, 119*(3), 839-847.

Lee, S. J., Seo, K. W., Choi, Y. S., & Sohn, M. H. (2011). Three-dimensional motion measurements of free-swimming microorganisms using digital holographic microscopy. *Measurement Science and Technology, 22*(6), 064004.

Liu, R., Dey, D. K., Boss, D., Marquet, P., & Javidi, B. (2011). Recognition and classification of red blood cells using digital holographic microscopy and data clustering with discriminant analysis. *JOSA A, 28*(6), 1204-1210.

Moon, I., Javidi, B., Yi, F., Boss, D., & Marquet, P. (2012). Automated statistical quantification of three-dimensional morphology and mean corpuscular hemoglobin of multiple red blood cells. *Optics Express, 20*(9), 10295-10309.

Pavillon, N., Kühn, J., Moratal, C., Jourdain, P., Depeursinge, C., Magistretti, P. J., & Marquet, P. (2012). Early cell death detection with digital holographic microscopy. *PloS one, 7*(1), e30912.

Schneider, B., Vanmeerbeeck, G., Stahl, R., Lagae, L., & Bienstman, P. (2015). *Using neural networks for high-speed blood cell classification in a holographic-microscopy flow-cytometry system.* Paper presented at the SPIE BiOS.

Shin, D., Daneshpanah, M., Anand, A., & Javidi, B. (2010). Optofluidic system for three-dimensional sensing and identification of micro-organisms with digital holographic microscopy. *Optics letters, 35*(23), 4066-4068.

Tamrin, K. F., & Rahmatullah, B. (2016). A review on noise suppression and aberration compensation in holographic particle image velocimetry. *Cogent Physics, 3*(1), 1142819.

Tamrin, K. F., Rahmatullah, B., & Samuri, S. M. (2014). *Astigmatism compensation in digital holographic microscopy using complex-amplitude correlation.* Paper presented at the 23rd Scientific Conference of the Microscopy Society Malaysia Perak, Malaysia.

Tamrin, K. F., Rahmatullah, B., & Samuri, S. M. (2015a). Aberration compensation of holographic particle images using digital holographic microscopy. *Journal of Modern Optics, 62*(9), 701-711.

Tamrin, K. F., Rahmatullah, B., & Samuri, S. M. (2015b). An experimental investigation of three-dimensional particle aggregation using digital holographic microscopy. *Optics and Lasers in Engineering, 68*, 93-103.

Tinmouth, A., Fergusson, D., Yee, I. C., & Hébert, P. C. (2006). Clinical consequences of red cell storage in the critically ill. *Transfusion, 46*(11), 2014-2027.

Wormald, S. A., & Coupland, J. (2009). Particle image identification and correlation analysis in microscopic holographic particle image velocimetry. *Applied optics, 48*(33), 6400-6407.

Yarnell, J., Baker, I., Sweetnam, P., Bainton, D., O'brien, J., Whitehead, P., & Elwood, P. (1991). Fibrinogen, viscosity, and white blood cell count are major risk factors for ischemic heart disease. The Caerphilly and Speedwell collaborative heart disease studies. *Circulation, 83*(3), 836-844.